separations

MDPI

Article

Mechanistic Insight into Ceramic Ball in Regrinding of Titanomagnetite Rougher

Jian Xu [1], Peixuan Li [1], Wenxia Zhu [1,*], Jianhua Kang [1,2,*] and Li Wang [1,2]

[1] School of Minerals Processing and Bioengineering, Central South University, Changsha 410083, China; 245612130@csu.edu.cn (J.X.); l15025107684@163.com (P.L.); li_wang@csu.edu.cn (L.W.)
[2] State Key Laboratory of Mineral Processing, Beijing 100160, China
* Correspondence: 245601011@csu.edu.cn (W.Z.); kangjianhua@csu.edu.cn (J.K.)

Abstract

Ceramic balls are utilized as grinding media for regrinding of titanomagnetite rougher, owing to its low liberation degree and intricate intergrowth with gangue minerals. Process mineralogy, regrinding experiments and EDEM simulations were adopted to investigate the influencing mechanism of ceramic balls on the regrinding performance of titanomagnetite rougher. The Dv(90) of titanomagnetite rougher is 198.19 μm, and the titanomagnetite is closely intergrown with gangue minerals, including chlorite, serpentine and ilmenite, in the forms of inclusions, interlocks and solid solutions with a liberation degree of 75.54%. The Dv(90) reduces to 39.86 μm, and the liberation degree of titanomagnetite increases to 92.86% after regrinding with ceramic balls. The grade was improved from 53.01% to 58.83% with a recovery of 96.19% after magnetic separation. EDEM simulation results reveal that raising stirrer speed elevated collision energy, increasing pulp density enhanced viscous coupling and particle capture, and improving media filling ratio boosted collision frequency. These findings demonstrate that ceramic balls could effectively refine product size, facilitate mineral liberation and improve concentrate grade, offering a viable pathway toward efficient utilization of titanomagnetite.

Keywords: vanadium–titanium magnetite; ceramic balls; regrinding; grinding kinetics; EDEM simulation

1. Introduction

Iron and steel constitute essential materials for modern industrial infrastructure, transportation, and national defense, and the technological advancement of the iron and steel industry directly shapes the pace of industrialization, manufacturing competitiveness, and supply-chain resilience [1–3]. The strategic importance of the steel industry has become even more pronounced amid the global commitments to carbon neutrality and industrial restructuring. However, China's indigenous iron ore resources are limited in both quantity and quality, rendering the country heavily dependent on imported raw materials. This structural vulnerability poses persistent risks to industrial security and macroeconomic stability for the domestic steel sector [4–6]. Therefore, exploiting domestic iron ore resources represents a strategic priority.

Among China's indigenous deposits, vanadium–titanium magnetite (VTM) resources, particularly those in Sichuan Province, constitute a significant polymetallic asset in which iron, vanadium, and titanium are closely associated [7]. In current industrial practice, VTM ores are processed using a combined magnetic separation–flotation flowsheet based

Check for updates

Academic Editor: Shuling Gao

Received: 26 July 2026
Revised: 14 August 2026
Accepted: 21 August 2026
Published: 23 August 2026

Copyright: © 2026 by the authors. Licensee MDPI, Basel, Switzerland. This article is an open access article distributed under the terms and conditions of the Creative Commons Attribution (CC BY) license.

on stage grinding and stage separation. Titanium is subsequently recovered from the magnetic tailings by flotation, enabling the co-extraction of iron and titanium values [8,9]. Nevertheless, these ores have inherent geological disadvantages: extremely fine mineral dissemination, complex interlocking textures, and abundant gangue impurities. Conventional separation routes produce iron concentrates of relatively low grade and high impurity content, which preclude their high-value downstream utilization [10–12].

To overcome the poor liberation caused by the intricate intergrowth of iron and titanium-bearing minerals in VTM ores, the prevailing industrial practice employs a stage regrinding step for the titanomagnetite rougher prior to magnetic separation. This step is designed to promote mineral liberation and enhance downstream separation efficiency [13–15]. Grinding, as the critical unit operation between crushing and beneficiation, accounts for a significant share of both capital and operating costs in mineral processing plants [16,17]. Grinding parameters, namely grinding duration, stirring speed, media filling ratio and pulp density, exert direct control over the particle size and particle size distribution of ground products. Meanwhile, by regulating mineral liberation degree, particle morphology and surface properties, these parameters indirectly govern the technical performance of downstream separation, dewatering processes and the final concentrate products [18,19]. Kutuk S et al. [20] systematically investigated how grinding parameters affect the particle size of ulexite, and elucidated the evolutionary patterns of particle size distribution and powder characteristics of ground products under diverse grinding conditions. Subsequent research by Kutuk-Sert T et al. [21] further revealed that the nanoscale effect of eco-friendly ultrafine ulexite powder substantially improves the pavement performance of stone mastic asphalt. This demonstrates that optimized regulation of grinding parameters can endow mineral powder materials with novel functional properties, thereby broadening their application scope.

For decades, metallic grinding media—predominantly high-chromium steel balls—have been the standard choice for both coarse and fine grinding, owing to their high specific gravity and strong impact action [22]. However, steel balls are subject to severe wear, which increases media consumption costs. Moreover, despite enabling high grinding throughput, small-diameter forged steel balls tend to induce overgrinding of the target minerals, thereby generating ultrafine particles. Overgrinding not only causes substantial losses of valuable metals but also complicates subsequent solid–liquid separation and impairs the selectivity of downstream beneficiation operations [23,24].

In recent years, zirconia-based ceramic balls have gained increasing recognition as high-performance fine-grinding media, owing to their low specific gravity, high hardness, and excellent wear resistance [25]. A growing body of research confirms that ceramic media offer distinct advantages in specific comminution settings because their characteristic collision mechanics and grinding modes can optimize the particle size distribution of the ground product [26]. Tong et al. [27] investigated how ceramic balls influence product particle size distribution and collision energy dissipation during grinding, and reported that ceramic balls generate far fewer ultrafine particles than steel balls, thereby mitigating overgrinding and reducing overall energy consumption. In subsequent work, Fang et al. [28] demonstrated that blending ceramic and steel media improves the breakage of coarse particles. This mixed-media configuration achieves grinding efficiency comparable to that of steel balls alone, while yielding substantial energy savings.

Despite the clear potential of ceramic media, implementing ceramic-ball regrinding in practice remains challenging: grinding is a dynamic process governed by multiphase interactions among media, particles, and the slurry phase. Media kinematics, collision characteristics, and energy dissipation are the principal variables controlling particle breakage, liberation, and overgrinding [29,30]. However, critical metrics such as media trajectory,

impact intensity, collision frequency, and energy loss are difficult to measure directly in real time under industrial or laboratory conditions [31]. The discrete element method (DEM), as implemented in EDEM 2022 (Altair Engineering, Inc.), has become an effective numerical tool for visualizing the motion and collision behavior of grinding media [32,33]. It permits quantitative calculation of collision velocity, collision force, collision frequency, and energy transfer efficiency, thereby overcoming the limitation of real-time measurement of media motion parameters during physical grinding experiments [34–36]. Combining EDEM simulations with grinding experiments provides robust support for elucidating the mechanisms by which grinding media influence the regrinding performance of the titanomagnetite rougher concentrate.

This study investigates a titanomagnetite rougher from Sichuan Province. Systematic mineralogical characterization was conducted to determine its mineral assemblage, disseminated grain size, and intergrowth features. Ceramic ball regrinding trials were then performed to quantify the effects of key operating parameters—grinding time, stirrer speed, media filling ratio, and pulp density—on the regrinding performance of the titanomagnetite concentrate. An EDEM model of media kinematics was developed, and the media velocity, number of collisions, and collision energy distribution were analyzed to elucidate the mechanisms governing regrinding performance. This work validates ceramic balls as effective regrinding media for a titanomagnetite rougher, clarifies their operating mechanisms, and provides a theoretical basis for optimizing regrinding circuits toward efficient and high-value exploitation of VTM resources.

2. Materials and Methods

2.1. Process Mineralogical Characterization

The titanomagnetite rougher utilized in this study was obtained from a VTM plant in Sichuan Province, China. Its mineralogical properties, including major element composition, mineral phase assemblage, particle size distribution, liberation degree, and intergrowth characteristics, were systematically characterized using a Mineral Liberation Analyzer (MLA; Changsha Research Institute of Mining and Metallurgy Co., Ltd., Changsha, China) Mineral Liberation Analyzer (MLA) and supplementary analytical techniques. All data were derived from MLA and its characterization techniques.

2.2. Regrinding and Magnetic Separation Tests

Prior to each grinding test, a 100 g portion of vanadium–titanium magnetite rougher was pre-screened on a 0.038 mm standard sieve, yielding an oversize (+0.038 mm) and an undersized (−0.038 mm) fraction. The oversize material was reground in a vertical stirred mill (JM-0.5A) using 3 mm diameter ceramic balls (95% zirconia) as the grinding media. The regrinding experiments were designed to investigate the influence of grinding time (2–6 min), mill speed (300–700 rpm), media filling ratio (20–60% by volume), and pulp density (30–70% solids by weight) on the regrinding performance. After grinding, the mill product was thoroughly blended with the undersize fraction, and the particle size distribution of the combined material was determined by laser diffraction. Magnetic separation was subsequently carried out with an XCGS-50 magnetic tube at a fixed magnetic field intensity of 0.14 T; the resulting magnetic concentrate and tailings were collected to determine the iron concentrate grade and recovery. The flowsheet for the grinding and magnetic separation tests is presented in Figure 1.

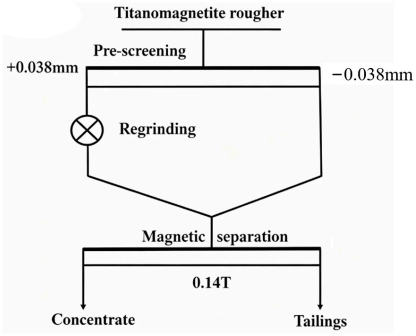

Figure 1. Flowsheet of regrinding and magnetic separation tests for the titanomagnetite rougher.

2.3. Grinding Kinetics Modeling

Grinding kinetics describes the mathematical relationship between particle breakage behavior and grinding time. The rate constant derived from the kinetic model provides a direct measure of the material's grinding response, enabling quantitative comparisons of grinding performance across different operating conditions. Grinding kinetics is commonly expressed as:

$$\frac{dR_i(t)}{dt} = -KR_i(t) \quad (1)$$

Integrating Equation (1) yields:

$$R_i(t) = (0)\ \exp\ (-Kt) \quad (2)$$

where $R_i(0)$ is the initial cumulative oversize fraction at size level i. Equation (2) corresponds to first-order kinetics. In practice, however, owing to ore heterogeneity, slurry rheology, and the prevailing grinding mechanisms, breakage kinetics often deviates from the first-order model and is better represented by the m-order expression:

$$R_i(t) = (0)\exp(-Kt^m) \quad (3)$$

where $R_i(t)$ is the cumulative oversize fraction (%), t is the grinding time (min), K is the characteristic grinding-rate parameter, and m is the uniformity index.

2.4. EDEM Simulation Conditions

Physical regrinding experiments provide only macroscopic particle size and separation indices, whereas the collision behavior and energy transfer processes of the ceramic balls inside the mill cannot be directly measured. Therefore, EDEM 2022 (Altair) discrete element software was used to construct a geometric model of the vertical stirred mill to elucidate the kinematic and dynamic mechanisms governing particle breakage. To reduce computational costs while capturing the essential inter-media collision and energy transfer mechanisms, reasonable simplifications were adopted for the numerical model. Only contact interactions between ceramic media particles and between media and the mill liner were incorporated. The liquid slurry and fine mineral particles were excluded, and drag forces induced by slurry viscosity as well as damping effects from ore particles during collisions were neglected. The simulation was therefore configured as a simplified dry-media system. Previous studies have demonstrated that DEM solid-particle models constructed without the slurry phase can reliably reproduce the flow characteristics of grinding balls in stirred mills [37]. In the present simulation, the abrasive wear of grinding media, mill chamber, and stirrer blades is not considered, and isothermal conditions are assumed; heat transfer and local overheating are neglected. This simplification is adopted because the present study focuses on the breakage behavior of ore particles and the milling time is relatively

short. Under these conditions, the effects of media wear and thermal phenomena are expected to be limited.

The motion of the grinding media was simulated using the discrete element method (DEM), and representative mill configurations at successive time steps are presented in Figure 2. All simulations were carried out in EDEM 2022 (Altair). A simplified mill geometry—comprising the mill chamber, the agitator shaft with discs, and the grinding media—was constructed in SolidWorks 2022 (Dassault Systèmes SolidWorks Corp., Waltham, MA, USA) based on the actual dimensions of the JM-0.5A vertical stirred mill (Changsha Tianchuang Powder Technology Co., Ltd., Changsha, Hunan, China) and subsequently imported into EDEM. The grinding media were modeled as spheres with a diameter of 3 mm, consistent with the ceramic balls used in the laboratory tests. The physical properties of the 3 mm zirconia ceramic balls—density, mass per ball, and specific surface area—were obtained from the manufacturer's official product specification sheet. Both particle–particle and particle–boundary interactions were described using the standard Hertz–Mindlin (no-slip) contact model, which is widely adopted in DEM studies of mineral processing systems. To ensure numerical stability, the time step was fixed at 20% of the Rayleigh time step. The total simulation duration was set to 3 s; the first 0.5 s was treated as a transient start-up period and discarded, and the steady-state data from 0.5 s to 3 s were averaged for subsequent analysis. All key simulation parameters are summarized in Table 1.

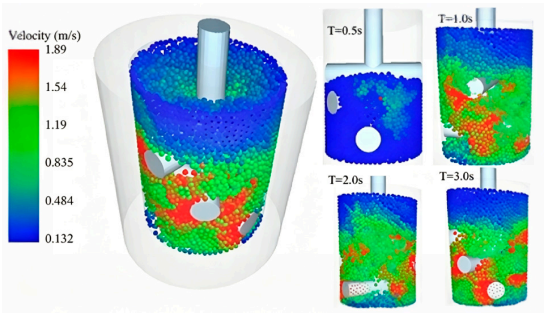

Figure 2. Dynamic distribution of ceramic grinding media at different simulation instants.

Table 1. Primary geometric and material parameters for EDEM simulation.

Parameter	Base Value
Mill height	11.9 cm
Internal diameter of the mill	9.5 cm
Stirrer diameter	1.5 cm
Stirring blade diameter	1.5 cm
Ball density	6000 kg/m^3
Ball mass	0.0848 g
Ball surface area	2.8×10^{-5} m^2
Equipment material solids density	7800 kg/m^3
Equipment material Poisson's ratio	0.3
Equipment material shear modulus	7×10^{10} Pa
Equipment material Young's modulus	1.82×10^{11} Pa
Rayleigh percentage	20%
Simulation time	3 s

3. Results and Discussion

3.1. Process Mineralogical Characteristics of Titanomagnetite Rougher

3.1.1. Iron Phase Analysis and Mineral Composition

Table 2 summarizes the iron phase distribution of the titanomagnetite rougher, which contains 53.01% total Fe. Titanomagnetite is the dominant iron-bearing phase, accounting for 87.28% of the total iron distribution with an iron content of 48.01%. Magnetite is the second most abundant iron phase, contributing 7.36% of the iron distribution at an iron content of 4.05%. Each of the remaining iron phases—limonite, ilmenite, iron sulfides, and silicates—accounts for less than 2% of the total iron distribution, while iron in carbonate minerals is negligible.

Table 2. Chemical phase analysis results of iron/%.

Iron Phases	Titanomagnetite	Magnetite	Silicates	Ilmenite	Iron Sulfides	Limonite	Carbonates
Content	48.01	4.05	1.63	0.66	0.52	0.12	0.02
Distribution	87.28	7.36	2.96	1.2	0.95	0.22	0.04

Table 3 presents the mineralogical composition of the rougher concentrate. Valuable minerals are dominated by titanomagnetite (79.81%), followed by magnetite (5.92%) and ilmenite (2.04%), which collectively account for 87.77% of the total sample. The main gangue phases are serpentine (2.85%), chlorite (2.84%), and olivine (1.60%), accompanied by minor pyroxene, amphibole, and feldspar. Serpentine and chlorite, both layered silicates, may impair subsequent grinding and separation efficiency.

Table 3. Main mineral composition and content/%.

Composition	Titanomagnetite	Magnetite	Serpentine	Chlorite	Ilmenite	Olivine
Content	79.81	5.92	2.85	2.84	2.04	1.6
Composition	Feldspar	Pyrrhotite	Pyroxene	Amphibole	Spinel	Others
Content	0.84	0.84	0.79	0.75	0.75	0.97

3.1.2. Intergrowth Characteristics and Particle Size Distribution of Titanomagnetite

The liberation characteristics and particle size distribution of titanomagnetite in the rougher concentrate were analyzed by MLA, and the results are presented in Table 4 and Figure 3, respectively. As shown in Table 4, titanomagnetite is predominantly intergrown with chlorite (37.96%), serpentine (18.78%), and ilmenite (14.42%), which together account for more than 70% of all intergrowth associations. Minor intergrowth associations include spinel, jarosite, amphibole, olivine, and other minerals, whereas associations with pyrrhotite, pyroxene, titanite, and feldspar are minor. Consequently, fine grinding is essential to liberate titanomagnetite grains locked within chlorite and serpentine, a prerequisite for improving concentrate quality. As shown in Figure 3, titanomagnetite exhibits a non-uniform fine- to media-grained grain size distribution with a relatively broad size range. The 0.21–0.037 mm fraction is dominant, representing a cumulative distribution of 66.87%, within which the 0.15–0.105 mm and 0.105–0.074 mm fractions display the highest individual proportions at 16.06% and 14.97%, respectively. The −0.037 mm fraction accounts for 23.98%, indicating a relatively high proportion of fine-grained titanomagnetite in the feed.

Table 4. Proportion of titanomagnetite intergrowths and interlocking minerals/%.

Composition	Chlorite	Serpentine	Ilmenite	Spinel	Iron alum	Amphibole	Olivine
Content	37.96	18.78	14.42	8.57	4.9	3.95	2.86
Composition	Pyrrhotite	Pyroxene	Titanite	Feldspar	Other minerals	Mica	Other metal sulfides
Content	1.9	1.77	1.63	1.36	0.96	0.54	0.41

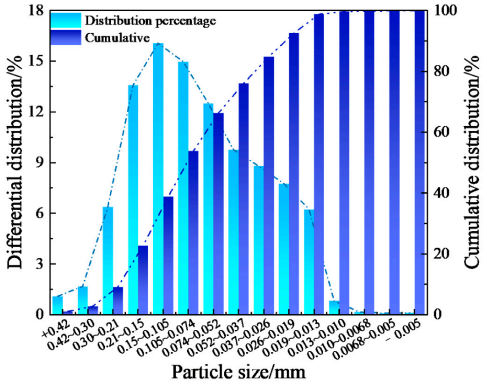

Figure 3. Size distribution of titanomagnetite.

3.1.3. Occurrence Morphology and Textural Features of Titanomagnetite

Backscattered electron imaging (Figure 4) reveals that titanomagnetite occurs predominantly as euhedral to subhedral equant grains, with irregular shapes and uneven size distribution in some grains. MLA analysis shows that approximately 75% of the titanomagnetite in the titanomagnetite rougher is fully liberated [38]. In locked particles, titanomagnetite is intergrown with chlorite, ilmenite, serpentine, and spinel, and less commonly associated with amphibole, jarosite, olivine, pyroxene, feldspar, pyrrhotite, and titanite. Texturally, grain margins are frequently intergrown with gangue minerals such as serpentine, olivine, and chlorite. In addition, titanomagnetite is present as inclusions alongside ilmenite, spinel, chlorite, and mica within host serpentine. Figure 5 presents backscattered electron images. Some titanomagnetite grains contain ilmenite lamellae or spinel microparticles exsolved from solid solution, together constituting a titanomagnetite-dominated composite assemblage. The grains host fine vein-like chlorite, flaky ilmenite, and granular spinel, while grain boundaries are intergrown with mica, feldspar, and amphibole. Flaky ilmenite occurs predominantly as fine exsolution precipitates within titanomagnetite, and granular ilmenite crystals themselves enclose fine spinel inclusions formed by exsolution. Additionally, some fine tabular ilmenite is closely associated with titanomagnetite and is embedded in a discrete gangue matrix composed primarily of amphibole and serpentine. This complex multiphase intergrowth texture strongly influences mineral liberation and subsequent separation performance.

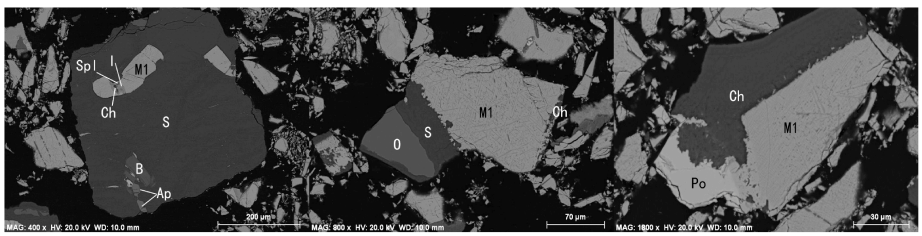

Figure 4. Backscattered electron images of titanomagnetite. M1-titanomagnetite; I-ilmenite; Spl-spinel; Ch-chlorite; S-serpentine; O-olivine; B-mica; Ap-apatite.

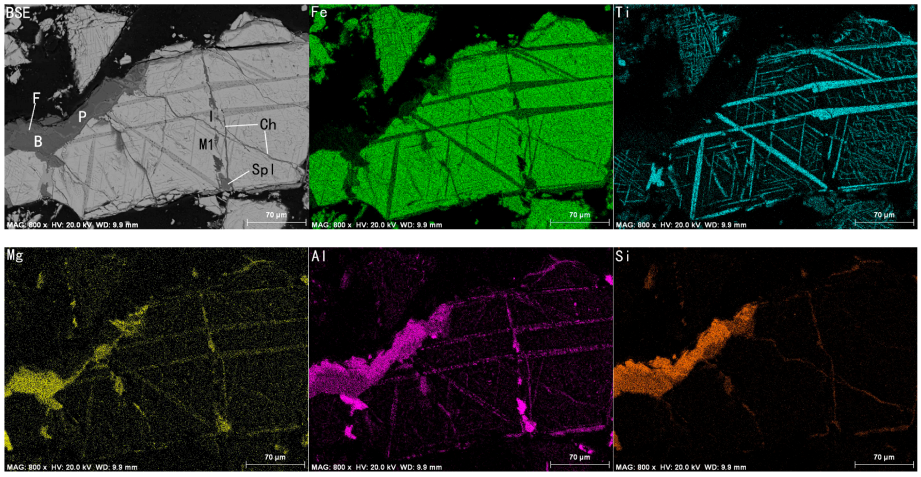

Figure 5. BSE images and EDS mapping of intergrowth characteristics of titanomagnetite. M1-titanomagnetite; I-ilmenite; Spl-spinel; Ch-chlorite; B-mica; P-feldspar; F-amphibole.

3.2. Regrinding Performance and Magnetic Separation Results

3.2.1. Effect of Grinding Time on Regrinding Performance

Grinding time strongly influences both the degree of mineral liberation and the risk of excessive fines generation. To study the effect of grinding time on the regrinding performance of ceramic balls, tests were conducted under fixed operating conditions: a pulp density of 50%, stirring speed 500 rpm, and filling ratio 50%. Figure 6 illustrates the evolution of particle size distribution as a function of grinding time. As grinding progressed, the particle size distribution shifted progressively toward finer fractions (Figure 6a), reflecting the cumulative effect of repeated impact and shear forces imparted by the ceramic media that disintegrate locked mineral aggregates. However, the size-reduction efficiency diminished markedly with time. The zirconia ceramic balls produced rapid particle size reduction within the first 5 min; beyond this point, the rate of size reduction declined sharply. After 6 min, Dv(50) and Dv(90) reached 16.68 μm and 59.78 μm, respectively (Figure 6b).

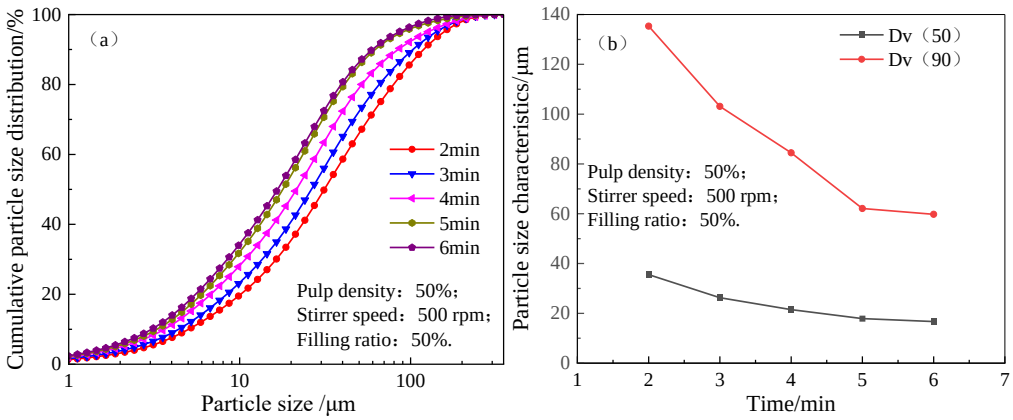

Figure 6. Influence of grinding time on particle size characteristics of reground titanomagnetite rougher. (**a**) Particle size distribution; (**b**) Dv(50) and Dv(90) variations.

The fitted residual mass curves and the corresponding kinetic parameters are presented in Figure 7 and Table 5, respectively. For all six size fractions, the coefficient of determination R^2 exceeded 0.97, indicating that the m-order kinetic model provides a satisfactory fit to the grinding behavior observed with ceramic balls. The grinding rate constant K exhibited a pronounced monotonic increase with particle size, rising from 0.0068 for the finest fraction (0.99 μm) to 0.5478 for the coarsest (45.60 μm). Coarse locked aggregates contain abundant

internal microcracks and intergranular weak planes, rendering them highly susceptible to fracture under repeated impact and shear loading. In contrast, liberated fine grains lack such natural fracture defects and strongly resist further comminution. The kinetic order coefficient m remained below unity for all size fractions and declined moderately with increasing particle size, signifying that the breakage rate decreases sub-linearly with grinding time. During the early stage of regrinding, coarse mineral aggregates with high grindability are rapidly fragmented, absorbing the majority of the grinding energy. As comminution proceeds, the feed becomes progressively dominated by hard-to-crush fine particles that absorb collision energy without undergoing appreciable size reduction [39,40]. Consequently, the overall breakage rate diminishes steadily, accounting for the progressive decline in refining efficiency evident in the particle size results.

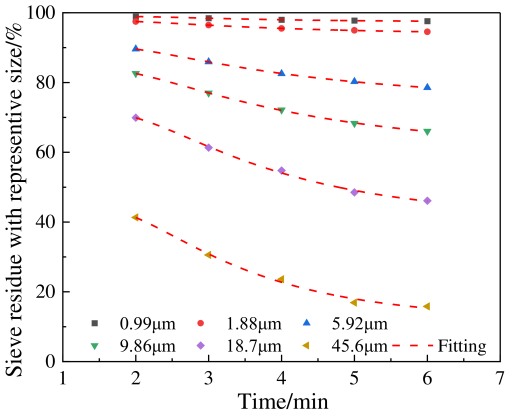

Figure 7. Cumulative residual and fitting curves for six representative screen sizes.

Table 5. Parameters of grinding kinetics equations for six representative screen sizes.

Parameter	0.99 μm	1.88 μm	5.92 μm	9.86 μm	18.70 μm	45.60 μm
K	0.0068	0.0158	0.0676	0.1181	0.2196	0.5487
M	0.7477	0.7341	0.728	0.7179	0.7217	0.6993
R^2	0.9786	0.9846	0.9936	0.9952	0.9942	0.9887

3.2.2. Effect of Stirrer Speed on Regrinding Performance

Stirrer speed determines the kinetic energy imparted to the ceramic balls and the intensity of particle–media collisions, thus governing the fragmentation efficiency of locked titanomagnetite aggregates. To elucidate how stirrer speed mediates particle refinement, tests were performed under fixed operating parameters: a pulp density of 50%, media filling ratio of 50%, and a constant grinding duration of 4 min. Figure 8 presents the particle size evolution across the tested speed range. Increasing the stirrer speed caused the cumulative particle size distribution curves to shift continuously toward finer fractions (Figure 8a). Previous studies have demonstrated that as the velocity and mobility of the grinding media increase, the kinetic energy transferred to the mineral particles increases accordingly. The resulting high-intensity collisions disrupt the mineral crystal structure, promoting particle size reduction and the liberation of intergrown minerals. This kinetic behavior has been verified in ultrafine grinding tests of ulexite [41]. Nevertheless, the comminution exhibited a clear threshold at 600 rpm. Significant particle size reduction was achieved when the speed was raised from 200 rpm up to 600 rpm, whereas further speed increments above this threshold yielded only marginal improvements in comminution. Quantitatively, Dv(50) and Dv(90) reached their minimum values of 13.97 μm and 39.86 μm, respectively, at the maximum tested speed of 700 rpm (Figure 8b); however, the incremental reduction in characteristic particle sizes diminished markedly once the stirrer speed exceeded 600 rpm.

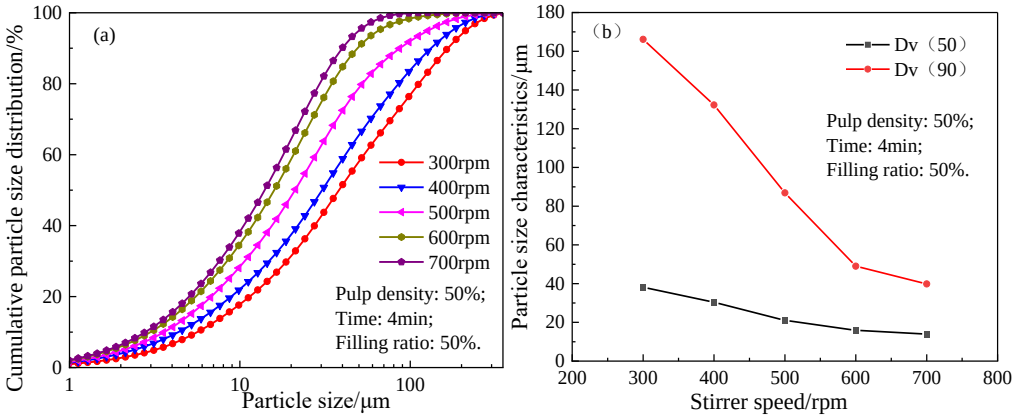

Figure 8. Influence of stirrer speed on particle size characteristics of reground titanomagnetite rougher. (**a**) Particle size distribution; (**b**) Dv(50) and Dv(90) variations.

The fitted residual mass evolution curves and corresponding kinetic parameters are summarized in Figure 9 and Table 6, respectively. All fitted datasets yielded a coefficient of determination R^2 above 0.96, indicating that the m-order kinetic model provides a satisfactory fit to the ceramic-ball comminution behavior within the tested stirrer speed interval. For all particle size fractions, elevated stirrer speed continuously lowered the residual oversize mass, and this size reduction was far more pronounced for coarse locked aggregates [42]. The grinding rate constant K increased monotonically with particle size, rising from 3.84×10^{-5} for the finest 0.99 μm fraction to 3.33×10^{-4} for the coarsest 45.60 μm fraction. As stirrer speed increased, ceramic media gained higher kinetic energy and underwent more frequent collisions, amplifying the intrinsic difference in breakage susceptibility between coarse and fine particles and leading to a pronounced reduction in residual coarse particle content. The kinetic order parameter m increased steadily from 0.978 to 1.491 with increasing particle size, indicating a transition from near-first-order to accelerated breakage kinetics. Fine particles follow breakage kinetics close to the first-order model, while coarse aggregates undergo accelerated fracture. Continuous high-energy impacts progressively propagate internal microcracks within coarse particles, further weakening their structural integrity and increasing their susceptibility to subsequent breakage [43,44]. This kinetic transition accounts for the threshold behavior at 600 rpm observed in the preceding particle size analysis.

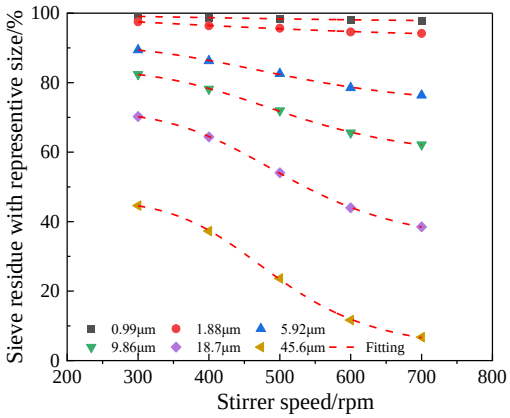

Figure 9. Cumulative residual and fitting curves for six representative screen sizes.

Table 6. Parameters of grinding kinetics equations for six representative screen sizes.

Parameter	0.99 μm	1.88 μm	5.92 μm	9.86 μm	18.70 μm	45.60 μm
K	3.84×10^{-5}	9.19×10^{-5}	1.47×10^{-4}	2.44×10^{-4}	2.93×10^{-4}	3.33×10^{-4}
M	0.978	1.033	1.074	1.107	1.232	1.491
R^2	0.985	0.987	0.996	0.991	0.9832	0.964

3.2.3. Effect of Filling Ratio on Regrinding Performance

The media filling ratio determines the total number of ceramic balls in the mill, directly affecting both the collision frequency and the mobility of individual media particles. To clarify how filling ratio mediates particle refinement, tests were conducted under fixed baseline conditions: a stirrer speed of 500 rpm, grinding time 4 min, and pulp density 50%. Figure 10 presents the resulting particle size distributions. Increasing the media filling ratio shifted the cumulative particle size distribution curves progressively toward finer fractions (Figure 10a), reflecting the enhanced frequency of shear and impact events that promote the breakage of locked particles. However, a clear threshold appeared at a filling ratio of 40%. Filling ratios below 40% yielded substantial particle size reduction, while further increases in media loading above this threshold brought only marginal improvements in comminution. Quantitative variations in characteristic particle sizes are plotted in Figure 10b: both Dv(50) and Dv(90) decreased monotonically with increasing media filling ratio, reaching minimum values of 19.97 μm and 79.51 μm, respectively, at the maximum tested filling ratio of 60%.

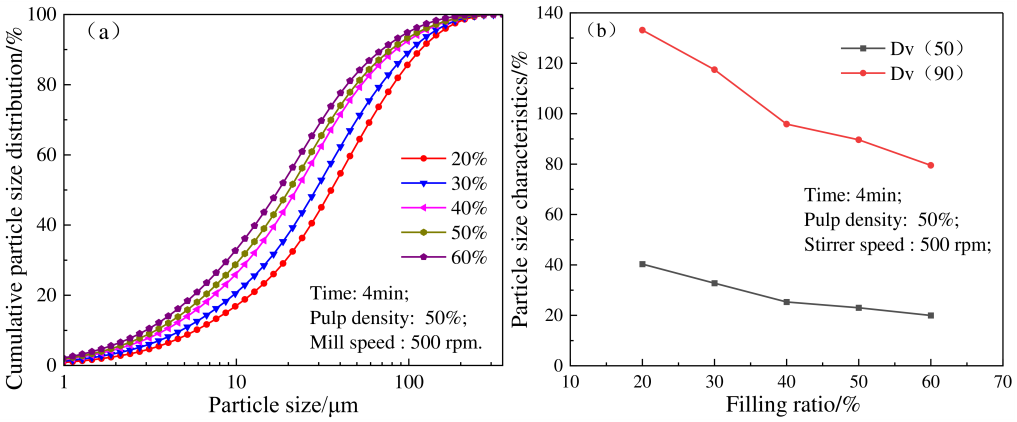

Figure 10. Influence of media filling ratio on particle size characteristics of reground titanomagnetite rougher. (**a**) Particle size distribution; (**b**) Dv(50) and Dv(90) variations.

The fitted residual mass evolution curves and corresponding kinetic parameters are summarized in Figure 11 and Table 7. All tested particle fractions yielded a coefficient of determination R^2 above 0.98, indicating that the m-order kinetic model provides an excellent fit to the ceramic-ball regrinding response across the entire filling-ratio range investigated. Increasing the media filling ratio reduced the residual oversize mass for all particle sizes, and this effect was much more pronounced for coarse locked aggregates than for fine liberated grains. The grinding rate constant K increased monotonically with particle size, ranging from 4.99×10^{-4} for the finest 0.99 μm fraction to 0.134 for the coarsest 45.60 μm fraction. Together with the pronounced reduction in residual coarse particle content, this trend indicates that coarse mineral aggregates are significantly more sensitive to variations in media filling ratio than fine liberated grains. Nevertheless, the marginal gains in breakage efficiency were gradually offset under excessively high filling ratios, as overcrowding suppressed single-collision intensity and weakened the fracture

force imparted to mineral particles. Unlike K, which increased monotonically with particle size, the kinetic order parameter m decreased monotonically as particle size increased, falling from 0.864 (0.99 μm) to 0.593 (45.60 μm). This monotonic decline suggests a shift in the dominant breakage mechanism: for fine particles, repeated low-energy collisions progressively expand internal microcracks, accumulating structural damage and sustaining accelerated fragmentation kinetics; for coarser particles, breakage increasingly relies on fewer, high-intensity impact events, leading to decelerated kinetics [45–47]. This restricted media mobility limited further dissociation of coarse particles, and the reduced cumulative fracture efficiency caused m to decline at high filling ratios.

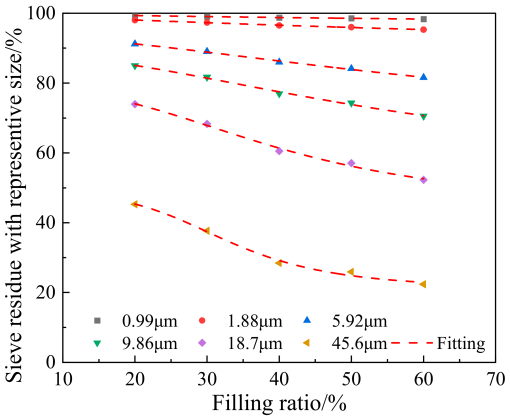

Figure 11. Cumulative residual and fitting curves for six representative screen sizes.

Table 7. Parameters of grinding kinetics equations for six representative screen sizes.

Parameter	0.99 μm	1.88 μm	5.92 μm	9.86 μm	18.70 μm	45.60 μm
K	4.99×10^{-4}	1.69×10^{-3}	1.03×10^{-2}	1.95×10^{-2}	3.59×10^{-2}	0.134
M	0.864	0.819	0.73	0.701	0.673	0.593
R^2	0.9973	0.9963	0.9964	0.9949	0.9924	0.9857

3.2.4. Effect of Pulp Density on Regrinding Performance

Pulp density governs slurry rheology, which in turn influences the probability of particle capture between colliding ceramic balls and affects the overall comminution performance of intergrown titanomagnetite grains. To clarify how pulp density alters particle refinement, tests were conducted under fixed baseline conditions: a stirring speed of 500 rpm, grinding time 4 min, and media filling ratio 50%. Figure 12 presents the particle size distributions obtained across the tested pulp density range. Increasing the pulp density shifted the cumulative particle size distribution curves continuously toward finer fractions (Figure 12a), indicating that a higher pulp density facilitates more effective particle fragmentation. Notably, the rate of size reduction exhibited a transition at a pulp density of approximately 50%. Mild particle size reduction was observed when the pulp density remained below 50%, whereas far more pronounced comminution occurred once it surpassed this threshold. Quantitative changes in characteristic particle sizes are plotted in Figure 12b: both Dv(50) and Dv(90) decreased monotonically with increasing pulp density, reaching minimum values of 16.6 μm and 69.3 μm, respectively, at the maximum tested value of 70%.

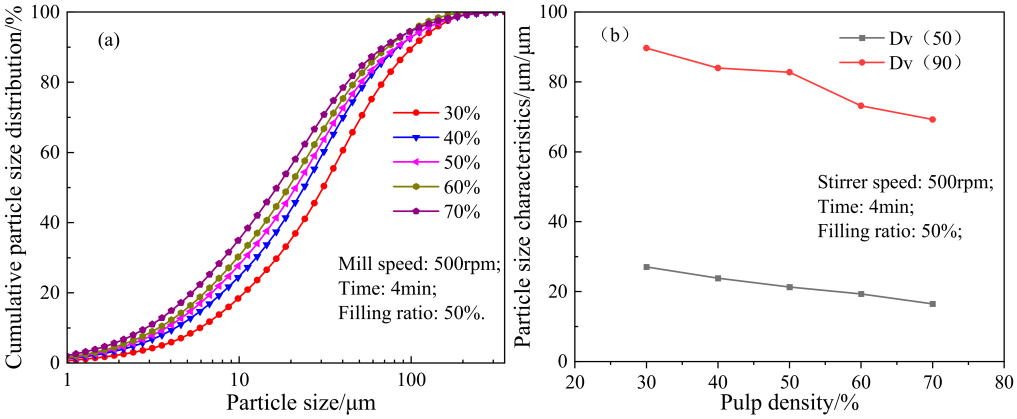

Figure 12. Influence of pulp density on particle size characteristics of reground titanomagnetite rougher. (**a**) Particle size distribution; (**b**) Dv(50) and Dv(90) variations.

The fitted residual mass evolution curves and corresponding kinetic parameters are summarized in Figure 13 and Table 8. All fitted datasets yielded a coefficient of determination $R^2 > 0.98$, indicating that the m-order kinetic model provides an excellent fit to the ceramic-ball regrinding response within the tested pulp-density range. For all particle size fractions, higher pulp density reduced the residual oversize mass, and this effect was most pronounced for the coarsest 45.60 μm fraction. The grinding rate constant K increased monotonically with particle size, rising from 3.25×10^{-4} for the finest 0.99 μm grains to 0.335 for the 45.60 μm coarse aggregates. Together with the substantial reduction in residual coarse particle content, this trend indicates that coarse locked titanomagnetite intergrowths are considerably more sensitive to adjustments in pulp density than liberated fine particles. Mechanistically, higher pulp density promoted closer particle packing within the gaps between colliding ceramic media, increasing the probability that large mineral aggregates are captured in the grinding zone and thereby facilitating their fracture. The kinetic order parameter m decreased monotonically from 0.969 for the 0.99 μm fraction to 0.694 for the 45.60 μm fraction, with all values remaining below unity. This systematic decline indicates that breakage follows decelerating kinetics across all sizes, but the deviation from first-order behavior becomes progressively more pronounced as particle size increases [48,49]. The near-unity m for the finest fraction points to damage accumulation through numerous low-energy contacts, whereas the substantially lower m for coarse aggregates suggests that their fracture is dominated by fewer, high-intensity impact events whose efficiency diminishes as the most susceptible particles are rapidly eliminated [50].

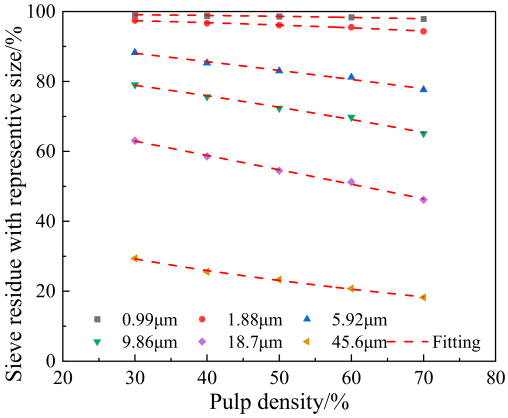

Figure 13. Cumulative residual and fitting curves for six representative screen sizes.

Table 8. Parameters of grinding kinetics equations for six representative screen sizes.

Parameter	0.99 μm	1.88 μm	5.92 μm	9.86 μm	18.70 μm	45.60 μm
K	3.25×10^{-4}	1.14×10^{-3}	8.24×10^{-3}	2.25×10^{-2}	6.04×10^{-2}	0.335
M	0.969	0.915	0.8618	0.799	0.735	0.6939
R^2	0.9848	0.9889	0.9893	0.9934	0.9957	0.9967

3.2.5. Magnetic Separation Performance of Reground Products

Table 9 and Figure 14 compare the liberation and size distribution of the titanomagnetite rougher before and after regrinding. Under the conditions—a grinding time of 4 min, stirrer speed 700 rpm, media filling ratio 50%, and pulp density 50%—the product exhibited a finer size distribution without generating excessive amounts of ultrafine particles. Dv(90) decreased from 198.19 μm to 39.86 μm, and Dv(50) from 64.23 μm to 13.97 μm, demonstrating substantial particle size reduction. The liberation degree increased markedly from 75.54% to 92.86%, and all other locked-particle categories declined, albeit to varying degrees, indicating the effective liberation of titanomagnetite from associated gangue phases [51,52].

Table 9. Liberation of titanomagnetite before and after regrinding/%.

Category	Liberated	Interlocked			
		>3/4	3/4~1/2	1/2~1/4	<1/4
Pre-grinding	75.54	12.61	8.02	2.75	1.08
Post-grinding	92.86	4.44	1.98	0.51	0.21

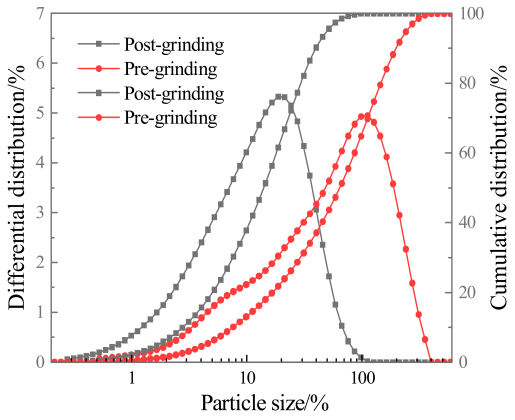

Figure 14. Particle size distribution comparison of titanomagnetite rougher before and after regrinding.

Table 10 and Figure 15 present the elemental composition and magnetic separation performance of the rougher concentrate before and after regrinding. As particle size decreased, the concentrate grade improved steadily, while iron recovery remained above 96% across all tested conditions. These results suggest that ceramic balls enhance concentrate quality by promoting liberation while suppressing overgrinding, thereby minimizing the formation of ultrafine magnetic particles that would otherwise be lost to the tailings during magnetic separation. Regrinding raised the total iron grade from 53.01% to 58.83% and reduced Mg, Si, Al, and S impurities to 2.54%, 1.01%, 1.70%, and 0.18%, respectively, while maintaining iron recovery above 96%, reflecting effective titanomagnetite–gangue liberation and the substantial removal of gangue and sulfide minerals.

Table 10. Major element variations in titanomagnetite rougher and reground magnetic concentrate/%.

Element	Fe	Ti	Mg	Si	Al	S
Titanomagnetite rougher	53.01	6.70	4.55	2.57	2.18	0.43
Titanomagnetite concentrate	58.83	7.04	2.54	1.01	1.70	0.18
Change	+5.82	+0.34	−2.01	−1.56	−0.48	−0.25

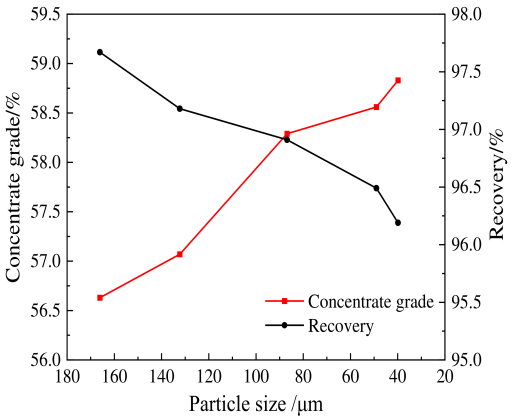

Figure 15. Magnetic separation performance of reground titanomagnetite concentrate with different fineness levels.

3.3. EDEM Simulation of Kinematic and Dynamic Characteristics of Ceramic Balls

3.3.1. Effect of Stirrer Speed on Ball Motion and Collision Behavior

To quantitatively elucidate the effect of stirrer speed on the rate of particle size reduction in regrinding tests, EDEM simulations were performed at a fixed pulp density of 50% and a media filling ratio of 50%. The resulting kinematic and dynamic outputs are presented in Figure 16. Improving the stirrer speed led to a steady increase in the relative collision velocity between ceramic balls, including both tangential and normal velocity components. The relative velocity rose from 0.11 m/s to 0.32 m/s, and the tangential velocity increased more significantly than the normal component (Figure 16a). Correspondingly, both normal and tangential collision forces intensified with increasing speed; the normal force increased more markedly, from 0.24 N to 0.50 N, while the tangential force increased only moderately from 0.09 N to 0.17 N. Although the tangential velocity component increased more, the tangential force was limited by the frictional coefficient and thus showed only a moderate rise. (Figure 16b). In contrast to collision velocity and force, the media–media collision frequency dropped sharply from 9.6×10^7 to 5.2×10^7, while media–wall collision counts remained consistently low with minimal variation across the full speed range (Figure 16c). Meanwhile, the total mechanical energy increased steadily from 45.20 J to 136.21 J, and this rise was predominantly attributable to kinetic energy, the proportion of which increased steadily with stirrer speed (Figure 16d).

These simulated parameters reveal that stirrer speed governs the dominant fragmentation mechanism. At low speeds, gentle stirring generates abundant low-energy collisions that promote breakage via shear and abrasion. At higher speeds, intensified agitation accelerates the ceramic media, markedly increasing collision velocity and impact force. Though collision frequency declines, the substantially enhanced normal impact force shifts the dominant mechanism toward impact-driven fragmentation [53,54]. However, at excessively high stirrer speeds (above 600 rpm), the centrifugal force inside the mill increases, causing a large proportion of media balls to adhere to the mill wall and decrease the regrinding efficiency. Consequently, ineffective friction and collision among the media intensify, thereby slowing the rate of particle size reduction. This media-motion transition explains the 600 rpm efficiency threshold identified in the regrinding analysis.

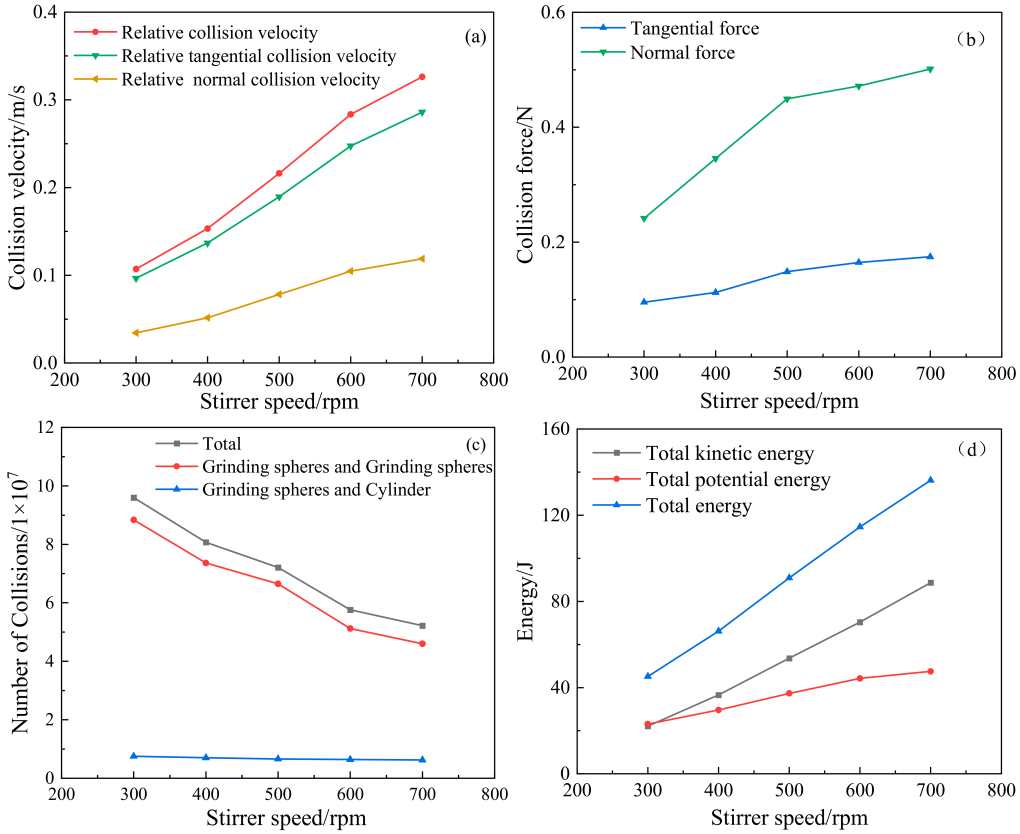

Figure 16. Effect of stirrer speed on kinematic and dynamic characteristics of ceramic ball: (**a**) collision velocity; (**b**) collision force; (**c**) collision frequency; (**d**) mechanical energy.

3.3.2. Effect of Pulp Density on Ball Motion and Energy Transfer

To quantitatively elucidate the effect of pulp density on the rate of particle size reduction in regrinding tests, EDEM simulations were conducted at a constant stirring speed (500 rpm) and media filling ratio (50%). The resulting kinematic and dynamic outputs are presented in Figure 17. Raising the pulp density led to a continuous increase in the relative collision velocity between ceramic balls, with both tangential and normal velocity components rising accordingly. The overall relative velocity rose from 0.15 m/s to 0.27 m/s, and the tangential component exhibited a greater increase than the normal counterpart (Figure 17a). Both normal and tangential collision forces increased with pulp density; the normal force rose from 0.32 N to 0.53 N, while the tangential force increased moderately from 0.11 N to 0.17 N (Figure 17b). Meanwhile, media–media collision frequency showed a modest increasing trend, whereas media–wall collision events remained negligible across the entire range (Figure 17c). The total mechanical energy increased gradually with pulp density; this increase was predominantly attributable to kinetic energy, which rose modestly, while potential energy showed minimal variation (Figure 17d).

Higher pulp density enhances momentum transfer between ceramic balls and slurry, minimizing relative slip and thereby increasing collision velocity and impact magnitude. The modest rise in collision frequency stems from narrowed inter-particle spacing and reduced gaps among ceramic balls; this tighter packing raises the probability of effective particle–media contact. The predominant increase in kinetic energy relative to potential energy further indicates that pulp density governs dynamic collision intensity [55,56]. Below a pulp density of 50%, low solids concentration fails to provide sufficient viscous coupling, resulting in inefficient momentum transfer and limited breakage. Above this threshold, higher pulp density ensures mineral particles are effectively captured between colliding beads, thereby enhancing the fracture energy imparted to locked aggregates. This

mechanistic explanation accounts for the pronounced size reduction and corresponding improvement in magnetic concentrate grade observed above 50% pulp density, indicating that appropriate pulp density simultaneously enhances both impact fracture and shear abrasion.

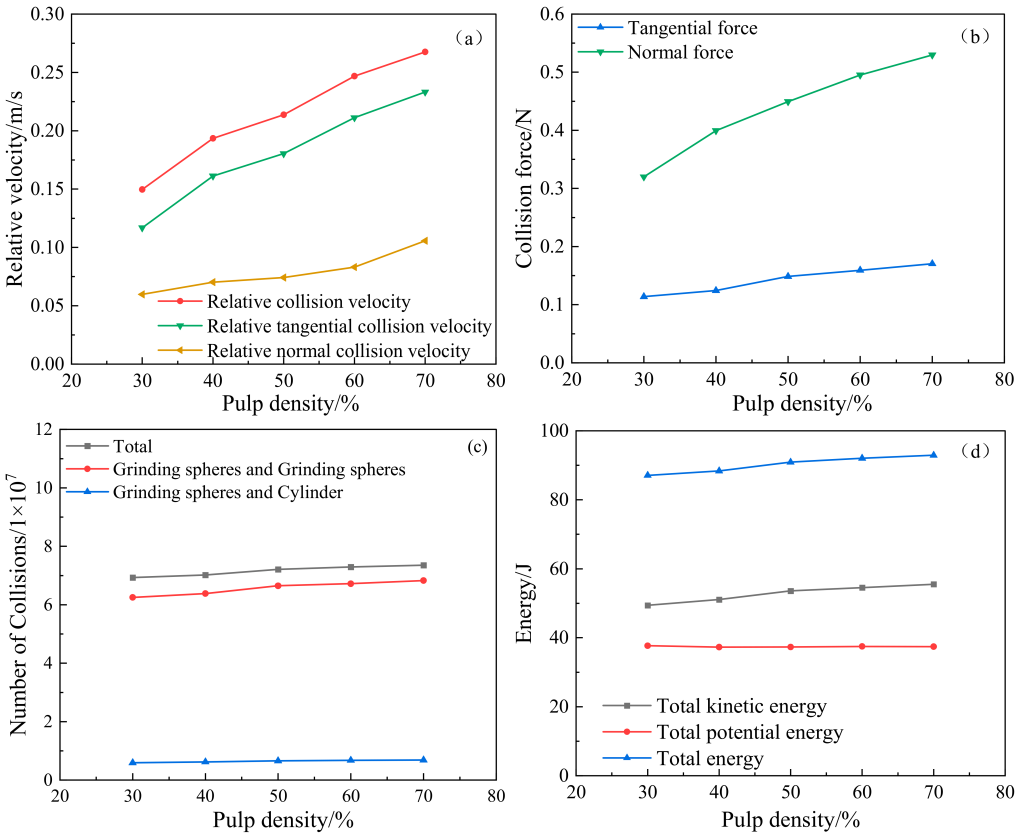

Figure 17. Effect of pulp density on kinematic and dynamic characteristics of ceramic media: (**a**) collision velocity; (**b**) collision force; (**c**) collision frequency; (**d**) mechanical energy.

3.3.3. Effect of Filling Ratio on Ball Collision and Energy Distribution

To quantitatively elucidate the effect of filling ratio on the rate of particle size reduction in regrinding tests, EDEM simulations were conducted at a constant stirrer speed (500 rpm) and pulp density (50%). The resulting kinematic and dynamic outputs are presented in Figure 18. Boosting the media filling ratio led to a monotonic decline in the relative collision velocity between ceramic balls, in both normal and tangential components. The overall relative collision velocity decreased from 0.29 m/s to 0.17 m/s (Figure 18a). Correspondingly, normal collision force declined from 0.46 N to 0.43 N, while tangential force decreased moderately from 0.16 N to 0.13 N (Figure 18b). In contrast, media–media collision frequency increased sharply from 1.22×10^7 to 1.05×10^8, while media–wall collision events showed a slight increase across all tested filling ratios (Figure 18c). The total mechanical energy increased steadily from 51.77 J to 100.58 J, with both kinetic and potential energy rising in parallel; notably, the proportion of kinetic energy rose steadily with increasing filling ratio (Figure 18d).

These results indicate that media filling ratio strongly influences collision behavior and energy distribution. Below a filling ratio of 40%, the limited number of ceramic balls provides sufficient mobility for high-velocity impacts that effectively fracture coarse locked aggregates. As the ratio exceeds 40%, the growing bead population substantially raises collision frequency, enhancing particle–media contact probability. Beyond this optimal range, however, excessive filling intensifies inter-bead crowding, restricting individual movement and reducing collision velocity and single-impact intensity. The associated

decline in normal impact force at high filling ratios signals a shift in the dominant breakage mechanism from impact fragmentation to high-frequency, low-intensity shear abrasion. While this regime still promotes mineral liberation, its efficiency in breaking coarse locked particles is substantially reduced. The simultaneous increase in both kinetic and potential energy indicates that the larger media population partially compensates for restricted individual mobility; however, this energy is distributed across more contacts, yielding lower energy per collision and consequently reduced fracture efficiency for coarse particles.

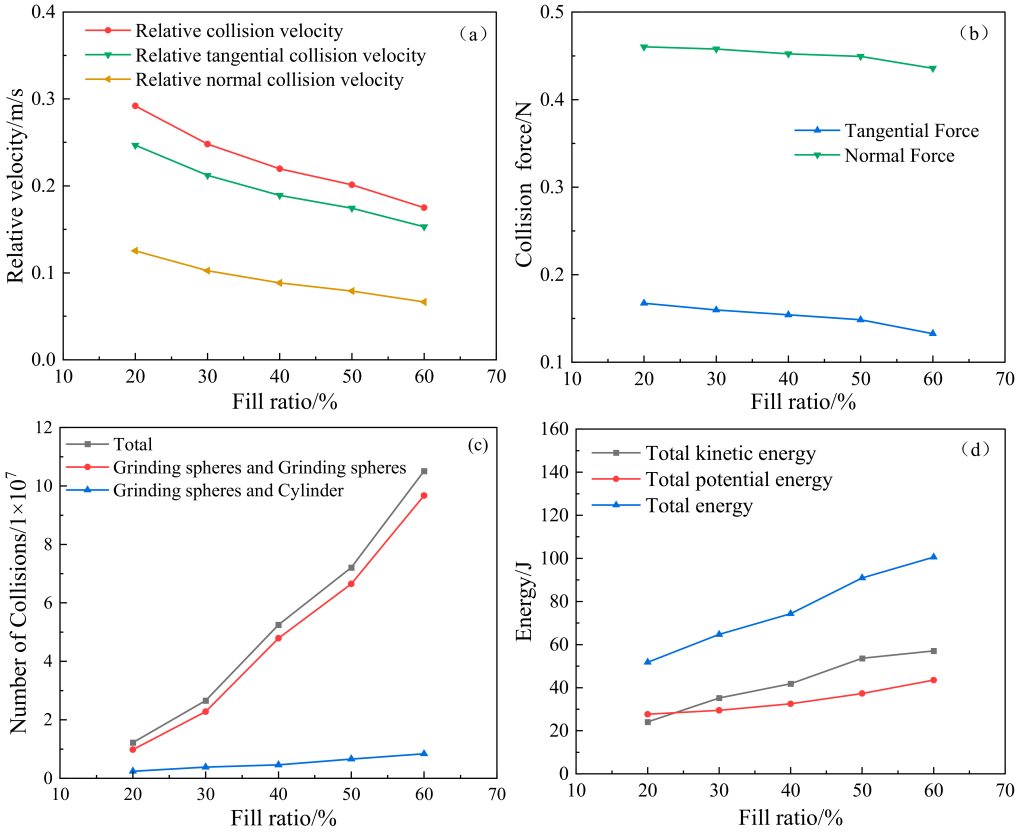

Figure 18. Effect of filling ratio on kinematic and dynamic characteristics of ceramic ball: (**a**) collision velocity; (**b**) collision force; (**c**) collision frequency; (**d**) mechanical energy.

4. Conclusions

This study investigated the effectiveness of ceramic balls as grinding media for the regrinding of a titanomagnetite rougher. By integrating process mineralogy, regrinding–magnetic separation tests, and EDEM simulations, the mechanisms governing ceramic-ball regrinding performance were elucidated. The results demonstrate that ceramic balls effectively promote mineral liberation, reduce particle size, and substantially improve concentrate grade while maintaining high recovery, offering a viable pathway toward the efficient utilization of VTM resources. The principal conclusions are as follows:

(1) Process mineralogical analysis revealed that the titanomagnetite rougher assays 53.01% Fe. Iron is predominantly hosted in titanomagnetite and magnetite, accounting for 87.28% and 7.36%, respectively. The feed exhibits a broad particle size distribution, with Dv(50) and Dv(90) of 64.23 μm and 198.19 μm, respectively, and the liberation degree of titanomagnetite is only 75.54%. A significant fraction of the locked particles is intimately intergrown with chlorite, serpentine, olivine, ilmenite, and spinel in the form of fine veinlet-like textures. This complex intergrowth architecture represents the primary mineralogical constraint limiting further improvements in concentrate grade and impurity rejection.

(2) Regrinding–magnetic separation tests showed that under the regrinding conditions—grinding time of 4 min, stirrer speed of 700 rpm, media filling ratio of 50%, and pulp density of 50%—the product exhibited a markedly finer size distribution without generating ultrafine particles. Specifically, Dv(90) decreased from 198.19 μm to 39.86 μm, and the liberation degree of titanomagnetite increased from 75.54% to 92.86%. Following magnetic separation, the iron grade of the concentrate improved from 53.01% to 58.83%, accompanied by substantial reductions in Si, Mg, and Al impurity contents, while recovery remained above 96%.

(3) EDEM simulations revealed that raising stirrer speed elevates collision velocity, collision force, and total kinetic energy, shifting the dominant breakage mechanism from shear-dominated abrasion to impact-dominated fragmentation. Increasing pulp density enhances viscous coupling between the media and the slurry, raising the collision frequency between ceramic balls and mineral particles and thereby improving regrinding efficiency. Improving the media filling ratio, while restricting the mobility of individual balls and reducing single-collision intensity, substantially elevates the overall collision frequency, leading to effective particle size reduction through cumulative low-intensity contacts. Collectively, these findings confirm that ceramic balls serve as effective regrinding media for titanomagnetite rougher, capable of enhancing mineral liberation, refining product size, and improving concentrate quality while sustaining high recovery. This study is of great significance for achieving efficient separation of VTM resources using ceramic balls as grinding media.

Author Contributions: Investigation, writing—original draft, visualization, J.X.; validation, investigation, P.L.; conceptualization, supervision, W.Z.; conceptualization, methodology, writing—review and editing, J.K.; resources, funding acquisition, L.W. All authors have read and agreed to the published version of the manuscript.

Funding: The research was supported by The National Key Research and Development Program of China (2023YFC2908302).

Data Availability Statement: Data is contained within the article.

Conflicts of Interest: The authors declare no conflicts of interest.

Abbreviations

The following abbreviations are used in this manuscript:

VTM	Vanadium–Titanium Magnetite
MLA	Mineral Liberation Analyzer
DEM	Discrete Element Method
EDEM	Engineering Discrete Element Method

References

1. Ren, M.; Zhu, B.; Huang, C.; Wang, J.; Dai, H. Multidimensional sustainability implications of alternative iron and steel industry decarbonization strategies in China. *Resour. Conserv. Recycl.* **2025**, *215*, 108136. [CrossRef]
2. Wang, H.F.; Qiu, J.; Ping, X.D.; Wang, F.; Lu, L.J.; Zhou, J.C.; Li, X.P. Roadmap, current situation, and prospects of low-carbon development technologies in Chinese steel industry. *J. Iron Steel Res. Int.* **2024**, *31*, 2879–2892. [CrossRef]
3. Tong, H.; Liu, J.; Wang, Y.; An, H.; Song, G.; Hou, Y.; Tang, X.; Yi, H. The transformation of China's iron and steel industry under carbon constraints: A balance between economy, emission reduction and technical feasibility. *J. Environ. Sci.* **2025**, *165*, 860–876. [CrossRef] [PubMed]
4. Liu, Z.; Dong, J.; Yan, L.; Han, G.; Zhang, L. Comprehensive Utilization Technology and Application of Total Resources from Ultra-Low-Grade Vanadium–Titanium Magnetite: A Case Study of Chengde, China. *JOM* **2026**. [CrossRef]
5. Qiao, Y.; Wang, G. Recent status of production, administration policies, and low-carbon technology development of China's steel industry. *Metals* **2024**, *14*, 480. [CrossRef]

6. Wei, W.; Zhou, D.; Chen, Z. The Current Situation, Development, and Prospects of the Iron and Steel Industry in the Process towards the "Dual Carbon" Goals. *Chin. J. Urban Environ. Stud.* **2023**, *11*, 2350009. [CrossRef]
7. Li, X.; Jiang, H.; Wang, Y.; Liu, G.; Chen, F.; Wu, N. The role of mineralogy study in the desulfurization flotation of vanadium-titanium magnetite. *Miner. Eng.* **2026**, *238*, 110045. [CrossRef]
8. Zhu, F.; Ma, Z.; Qiu, K.; Peng, W. Separation of ilmenite from vanadium titanomagnetite by combining magnetic separation and flotation processes. *Separations* **2023**, *10*, 95. [CrossRef]
9. Yu, H.D.; Wang, L.N.; Qu, J.K.; Qi, T. Process mineralogical characteristics and ore value of typical vanadium titanium magnetite in China. *J. Northeast. Univ. Nat. Sci.* **2020**, *41*, 275–281.
10. Zhu, F.; Ma, Z.; Gao, G.; Qiu, K.; Peng, W. Process mineralogy of vanadium titanomagnetite ore in Panzhihua, China. *Separations* **2023**, *10*, 147. [CrossRef]
11. Li, W.; Fu, G.; Chu, M.; Zhu, M. An effective and cleaner process to recovery iron, titanium, vanadium, and chromium from Hongge vanadium titanomagnetite with hydrogen-rich gases. *Ironmak. Steelmak.* **2021**, *48*, 33–39. [CrossRef]
12. Zhang, Z.; Huang, F.; Li, Y.; Liu, K.; Zhao, F. Nano-micron exsolved spinels in titanomagnetite and their implications for the formation of the Panzhihua Fe–Ti–V oxide deposit, southwest China. *J. Nanosci. Nanotechnol.* **2021**, *21*, 326–342. [CrossRef] [PubMed]
13. Zhong, X.; Hu, H.; Li, S.; Gao, J.; Shi, Z.; Zhu, F. Mineralogical characteristics of Baima vanadium titanomagnetite during magnetic separation upgrading. *Separations* **2023**, *10*, 574. [CrossRef]
14. Liu, J.; Xing, Z.; Cheng, G.; Xue, X.; Ding, X. Study on the grinding kinetics and magnetic separation of low-grade veneniferous titanomagnetite concentrate. *Metals* **2022**, *12*, 575. [CrossRef]
15. Tian, P.; Gao, P.; Tang, Z.; Zhang, Z.; He, J.; Wang, X.; Han, Y. Optimization of grinding parameters and efficient separation of iron and rare earths from poor oxide ores in magnetic separation operation. *Powder Technol.* **2025**, *458*, 120962. [CrossRef]
16. Abdelhaffez, G.S.; Ahmed, A.A.; Ahmed, H.M. Effect of grinding media on the milling efficiency of a ball mill. *Min.-Geol.-Pet. Eng. Bull.* **2022**, *37*, 171–177. [CrossRef]
17. da Conceição, C.D.; Santos, A.L.A.; Campos, L.J.F.; Bergerman, M.G.; Mazzinghy, D.B. Assessing the specific energy for two iron ores using steel, ceramic and mixed steel-ceramic ball charges in fine grinding. *Miner. Eng.* **2026**, *240*, 110077. [CrossRef]
18. Guo, M.; Yang, Y.; Yu, S.; Wu, Y.; Gu, G.; Wang, Y.; Li, Q.; Chen, J. Effects of Grinding Parameters on Galena Particle Size Distribution and Flotation Performance. *Minerals* **2025**, *15*, 618. [CrossRef]
19. Ma, S.; Li, H.; Shuai, Z.; Yang, J.; Deng, X.; Xu, W. Research on grinding law and grinding parameters optimization of polymetallic complex ores. *Minerals* **2022**, *12*, 1283. [CrossRef]
20. Kutuk, S. Influence of milling parameters on particle size of ulexite material. *Powder Technol.* **2016**, *301*, 421–428. [CrossRef]
21. Kutuk-Sert, T.; Kutuk, S.; Yentimur, M.F.; Sinoforoglu, F. Nano-size effect of environmentally friendly ulexite powder as a bitumen additive in stone mastic asphalt. *Eng. Sci. Technol. Int. J.* **2026**, *76*, 102328. [CrossRef]
22. Aldrich, C. Consumption of steel grinding media in mills—A review. *Miner. Eng.* **2013**, *49*, 77–91. [CrossRef]
23. Hassall, P.; Nonnet, E.; Keikkala, V.; Komminaho, T.; Kotila, L. Ceramic bead behavior in ultra fine grinding mills. *Miner. Eng.* **2016**, *98*, 232–239. [CrossRef]
24. Fang, X.; Wu, C.; Liao, N.; Yuan, C.; Xie, B.; Tong, J. The first attempt of applying ceramic balls in industrial tumbling mill: A case study. *Miner. Eng.* **2022**, *180*, 107504. [CrossRef]
25. Tong, J.; Tian, J.; Wang, Y.; Yao, X.; Li, Z.; Xir, F.; Wu, C.; Zeng, G.; Xu, J. Study on optimization parameters for ceramic ball of magnetite-quartz mixed system by response surface methodology. *Chin. J. Process Eng.* **2024**, *24*, 726–733.
26. Wu, C.; Chen, Z.; Liao, N.; Zeng, C.; Wang, Y.; Tian, J. Enhancing the grinding efficiency of a Magnetite second-stage mill through ceramic ball optimization: From laboratory to industrial applications. *Minerals* **2024**, *14*, 160. [CrossRef]
27. Tong, J.; Wu, C.; Wang, Y.; Tian, J.; Li, Z.; Xie, F.; Yao, X.; Zeng, G. Effect on fine particles output characteristics of ceramic ball grinding. *Minerals* **2023**, *13*, 1416. [CrossRef]
28. Fang, X.; Wu, C.; Yuan, C.; Liao, N.; Chen, Z.; Li, Y.; Lai, J.; Zhang, Z. Can ceramic balls and steel balls be combined in an industrial tumbling mill. *Powder Technol.* **2022**, *412*, 118020. [CrossRef]
29. Li, Y.; Liao, N.; Wu, C.; Lin, Z.; Luo, C.; Wu, H.; Zhou, J.; Huang, J. Effect of different size ceramic balls on quartz grinding dynamics in batch ball mill. *Particuology* **2025**, *102*, 141–151. [CrossRef]
30. de Carvalho, R.M.; Oliveira, A.L.; Petit, H.A.; Tavares, L.M. Comparing Modeling Approaches in Simulating a Continuous Pilot-Scale Wet Vertical Stirred Mill Using PBM-DEM-CFD. *Adv. Powder Technol.* **2023**, *34*, 104135. [CrossRef]
31. Yin, Z.; Zhang, Y.; Zhu, H.; Ding, H.; Wu, Q.; Zhu, Z.; Song, J. Optimization and experimental study of iron ore grinding medium parameters using EDEM discrete element Software. *Materials* **2024**, *17*, 4726. [CrossRef] [PubMed]
32. Muanpaopong, N.; Davé, R.; Bilgili, E. A comparative analysis of steel and alumina balls in fine milling of cement clinker via PBM and DEM. *Powder Technol.* **2023**, *421*, 118454. [CrossRef]
33. Yuan, C.; Wu, C.; Fang, X.; Liao, N.; Tong, J.; Li, Y. A new approach to the grinding kinetics of magnetite ore based on the population balance model. *Minerals* **2023**, *13*, 424. [CrossRef]

34. Liu, Z.; Wang, S.; Li, Y.; Mao, Y.; Ding, H.; Wu, S.; Xie, P.; Huang, Q. Analysis of Grinding Media Motion Behavior in a Vertical Spiral Stirred Mill Based on Discrete Element Method. *Granul. Matter* **2025**, *27*, 87. [CrossRef]
35. Qu, T.; Ma, L.; Song, X.; Wang, Z.; Zhang, S.; Zhao, Y.; Ji, H. Coupling simulation method and experiment of vertical stirring mill based on DEM–CFD. *Conserv. Util. Miner. Resour.* **2025**, *45*, 15–22.
36. Gu, R.; Wu, W.; Zhao, S.; Ma, Z.; Wang, Q.; Qin, Z.; Wang, Y. Kinematics and Dynamics Behavior of Milling Media in Vertical Spiral Stirred Mill Based on DEM-CFD Coupling. *Minerals* **2025**, *16*, 24. [CrossRef]
37. Govender, I.; Cleary, P.W.; Mainza, A.N. Comparisons of PEPT derived charge features in wet milling environments with a friction-adjusted DEM model. *Chem. Eng. Sci.* **2013**, *97*, 162–175. [CrossRef]
38. Blannin, R.; Frenzel, M.; Tuşa, L.; Birtel, S.; Ivăşcanu, P.; Baker, T.; Gutzmer, J. Uncertainties in quantitative mineralogical studies using scanning electron microscope-based image analysis. *Miner. Eng.* **2021**, *167*, 106836. [CrossRef]
39. Yuan, C.; Wu, C.; Ling, L.; Yao, X.; Li, Z.; Xie, F.; Tian, J. Ceramic grinding kinetics of fine magnetite ores in the batch ball mill. *Minerals* **2023**, *13*, 1188. [CrossRef]
40. Guven, O.; Bayar, G.; Sivrikaya, O.; Ulusoy, U. Investigation of the relationship between particle shape and flotation kinetic constants of magnetite ore ground in a ball mill at different grinding times. *Powder Technol.* **2026**, *474*, 122272. [CrossRef]
41. Kutuk, S. Morphology, crystal structure and thermal properties of nano-sized amorphous colemanite synthesis. *Arab. J. Sci. Eng.* **2024**, *49*, 11699–11716. [CrossRef]
42. Peng, J.; Wang, J.; Zhou, F.; Jiang, X.; Lin, R.; Zhao, Z.; Zhong, J. Influence of process parameters on motion characteristics and heat transfer in green tea powder grinding. *Adv. Powder Technol.* **2026**, *37*, 105258. [CrossRef]
43. Cayirli, S.; Gokcen, H.; Yuce, N. The impact of different stirrer designs and mill orientations on the grinding efficiency. *Powder Technol.* **2024**, *438*, 119577. [CrossRef]
44. Akkaya, B.; Toroğlu, İ.; Bilen, M. Studying the effect of different operation parameters on the grinding energy efficiency in laboratory stirred mill. *Adv. Powder Technol.* **2020**, *31*, 4517–4525. [CrossRef]
45. Ling, L.; Yuan, C.; Sun, L.; Wu, C.; Li, Q.; Zhou, Z.; Zhou, Z. Effect of Ball Filling Ratio on Fine Particle Production Characteristics During Ceramic Ball Grinding of Magnetite Ore. *Minerals* **2026**, *16*, 256. [CrossRef]
46. Elbendari, A.; Chen, Y.; Fengjing, W.; He, D. Effect of Ball Size and Ball Filling on the Breakage Kinetics of Fluorspar in a Ball Mill. *JOM* **2026**. [CrossRef]
47. Guo, W.; Han, Y.; Li, Y.; Tang, Z. Impact of ball filling rate and stirrer tip speed on milling iron ore by wet stirred mill: Analysis and prediction of the particle size distribution. *Powder Technol.* **2021**, *378*, 12–18. [CrossRef]
48. Inam, M.A.; Ouattara, S.; Frances, C. Effects of concentration of dispersions on particle sizing during production of fine particles in wet grinding process. *Powder Technol.* **2011**, *208*, 329–336. [CrossRef]
49. Yuan, C.; Wu, C.; Fang, X.; Liao, N.; Tong, J.; Yu, C. Effect of Slurry Concentration on the Ceramic Ball Grinding Characteristics of Magnetite. *Minerals* **2022**, *12*, 1569. [CrossRef]
50. Guo, W.; Guo, K. Effect of solid concentration on particle size distribution and grinding kinetics in stirred mills. *Minerals* **2024**, *14*, 720. [CrossRef]
51. Xiao, Q.; Li, B.; Kang, H. The effect of fine grinding medium feature on grinding results. *AASRI Procedia* **2014**, *7*, 120–125. [CrossRef]
52. Zhou, S.; Wang, Y.; Zheng, X.; Lu, D. Upgrading of ilmenite flotation concentrate by high gradient magnetic separation coupling with magnetic fluid: Removal of silicon and calcium impurities. *Miner. Eng.* **2026**, *235*, 109878. [CrossRef]
53. Kosaku, Y.; Tsunazawa, Y.; Okuyama, K.; Iwamoto, M.; Sekine, Y.; Tokoro, C. Investigation of optimum scale-up of media stirred mill using the discrete element method. *Mater. Trans.* **2022**, *63*, 1501–1509. [CrossRef]
54. Guo, W.; Gao, P.; Tang, Z.; Han, Y.; Meng, X. Effect of grinding media properties and stirrer tip speed on the grinding efficiency of a stirred mill. *Powder Technol.* **2021**, *382*, 556–565. [CrossRef]
55. Ibrahim, S.; Wong, S.; Baker, I.; Zamzam, Z.; Sato, M.; Kato, Y. Influence of geometry and slurry properties on fine particles suspension at high loadings in a stirred vessel. *Chem. Eng. Res. Des.* **2015**, *94*, 324–336. [CrossRef]
56. Ren, Y.; Zhao, L.; Mo, X.; Zheng, S.; Yang, Y. Coupled CFD-DEM Numerical Simulation of the Interaction of a Flow-Transported Rag with a Solid Cylinder. *Fluid Dyn. Mater. Process.* **2024**, *20*, 1593–1609. [CrossRef]

Disclaimer/Publisher's Note: The statements, opinions and data contained in all publications are solely those of the individual author(s) and contributor(s) and not of MDPI and/or the editor(s). MDPI and/or the editor(s) disclaim responsibility for any injury to people or property resulting from any ideas, methods, instructions or products referred to in the content.